Capabilities and limitations of existing finite element simplified micro-modeling techniques for unreinforced masonry

Nitin Kumar, Michele Barbato, Erika L. Rengifo-López, Fabio Matta

Research Article

Capabilities and limitations of existing finite element simplified micro-modeling techniques for unreinforced masonry

Nitin Kumar[*1,a], Michele Barbato[1,b], Erika L. Rengifo-López[2,c], Fabio Matta[2,d]

[1]Department of Civil and Environmental Engineering, University of California, Davis, U.S.A.
[2]Department of Civil and Environmental Engineering, University of South Carolina, Columbia, U.S.A.

Article Info	Abstract
	Finite element (FE) simplified micro-modeling techniques are commonly used to investigate and predict the mechanical behavior of masonry structures because they provide a good compromise between accuracy and computational cost. These FE techniques generally discretize masonry structural elements into expanded masonry units and zero-thickness interface joints of assumed known locations. These joints correspond to actual masonry joints and to preferential cracking surfaces, which are often placed vertically in the middle of the expanded masonry units to simulate the cracking mechanisms that are typically observed in masonry bricks and blocks. Three different versions of simplified micro-models (SMMs) are widely used in the literature to model the response of masonry walls and assemblies: SMMs with rigid, elastic, and elasto-plastic constitutive models for the expanded masonry units. All SMMs are based on the hypothesis that the masonry inelastic behavior and cracking are concentrated along the pre-defined zero-thickness interface joints. The hypothesis is often satisfied for ordinary masonry, in which masonry units are generally stronger than the masonry joints, i.e., mortar and unit-mortar interface. However, this hypothesis is not always satisfied for historical masonry with units of irregular shapes or for earth block masonry, in which masonry units and masonry joint can have similar mechanical properties. This paper highlights the capabilities and limitations of SMM techniques by comparing the experimentally-measured and numerically-simulated response of ordinary and earth block masonry walls, for which well-documented experimental results are available in the literature. It is found that SMMs can properly reproduce the mechanical behavior of masonry when the masonry units are significantly stronger than the masonry joints; however, SMMs produce poor estimates of the mechanical response when this hypothesis is not satisfied. This finding highlights the need to develop more general FE models to investigate the mechanical behavior of different masonry materials and construction techniques, as well as to identify the parameters controlling the cracking patterns and the conditions under which SMM techniques can be accurately use.

1. Introduction

Over the last three decades, finite element (FE) simplified micro-modeling techniques have been commonly employed to investigate the local and global mechanical response of masonry structures [1-12]. Simplified micro-models (SMMs) have been used as a computationally efficient alternative to detailed micro-models, which require the FE discretization of all masonry constituents, i.e., masonry units (bricks or blocks), mortar layers, and unit-mortar interfaces, and have been used only for small masonry components due to their high computational cost [13–19]. In SMMs, the mortar joint and the two

*Corresponding author: ntnkumar@ucdavis.edu
[a] orcid.org/0000-0002-4045-300X; [b] orcid.org/0000-0003-0484-8191; [c] orcid.org/0000-0002-2136-2639; [d] orcid.org/0000-0001-7018-6611

adjacent unit-mortar interfaces (referred to as masonry joints hereinafter) are lumped into zero-thickness interfaces (referred to as masonry joint interfaces hereinafter), which connect expanded masonry units (with dimensions equal to those of the masonry unit and half of the mortar thickness) [20]. In addition, a zero-thickness interface (referred to as potential crack interface hereinafter), is vertically placed in the middle of the expanded masonry units to simulate the potential cracking mechanism that is often experimentally observed in masonry units [20]. Based on the different constitutive models adopted for the expanded masonry units, three SMMs are commonly found in the literature, i.e., SMMs with rigid (referred to SMM-I hereinafter), elastic (referred to SMM-II hereinafter), and inelastic (referred to SMM-III hereinafter) constitutive models for the expanded masonry units.

Early uses of SMMs did not include potential-crack elements [16,21], which were introduced only later to better describe the experimental behavior of unreinforced masonry [22,23]. Lourenço and Rots [6] proposed an SMM-II approach in which the response of the interface elements was described by a three-surface interface constitutive model based on softening plasticity. This constitutive model could simulate shear sliding, tensile cracking, and compressive crushing, and was later extended, based on plasticity theory, to simulate the cyclic response of masonry structures [10] in many different applications [24–31]. Macorini and Izzuddin [4] proposed a three-dimensional two-surface interface constitutive model that used a co-rotational approach to account for geometric nonlinearity. This model has also been widely used for numerical modeling of masonry structures [32–34], and has been extended based on a damage-plasticity framework to simulate the cyclic behavior of masonry [35]. More recently, Kumar and Barbato [5] proposed a new three-dimensional two-surface interface constitutive model with improved computational efficiency and robustness. Other SMM-II approaches available in literature are based on different interface constitutive models based on damage and friction [36–39], elasto-plasticity [2,3,12], damage-plasticity [35,40], softening fracture [41], and viscoplasticity [42]. More recently, SMM-I [31] and SMM-III approaches [43–46] have been developed to simulate the cyclic behavior of masonry systems. Bolhassani et al. [47] also used an SMM-III approach to investigate the nonlinear behavior of hollow and partially grouted concrete block masonry walls using a damage-plasticity traction–separation law for the masonry joint interfaces, and a damage-plasticity continuum constitutive model for expanded masonry units. The SMM-I was originally introduced to reduce the number of models' degrees-of-freedom and the corresponding computational time; however, subsequent developments of the SMM-I lead to its most common use within a discrete element method framework [48–52].

The major assumption of existing SMMs is that most of the inelastic behavior of a masonry wall is concentrated at known locations that can be modeled using interface elements, i.e., at the masonry joint and potential crack interfaces [6]. This basic assumption is valid only when (1) the geometry of masonry units and mortar joints is regular (i.e., the masonry units have a uniform cuboid shape and the mortar layers have uniform thickness), and (2) the masonry units are significantly stronger in compression and shear than the masonry joints (i.e., for masonry built with fired clay bricks, concrete blocks, or regularly shaped stones [11]). However, specific instances exist in which the compressive and shear strengths of masonry units is similar to or smaller than those of the masonry joints, e.g., in earth block masonry, for which significant cracking through the earth blocks has been experimentally observed [53]. To the authors' knowledge, the only study available in the literature that employed SMMs to reproduce the mechanical response of earth block masonry did not achieve an accurate match between experimental and numerical results when using the experimentally-measured modeling parameters [25]. The same study was able to numerically reproduce the experimental results only after modifying the modeling parameter values through a numerical parametric study.

This paper investigates the capabilities and limitations of different SMMs by comparing their relative performance for two different types of masonry, i.e., fired-clay brick (FCB) and compressed and stabilized earth block (CSEB) masonry. After describing the different SMMs, this paper provides recommendations on constitutive models, FE solvers, and discretization requirements for FE SMMs of unreinforced masonry. Appropriate error measures are suggested to facilitate this comparison. Two benchmark examples are investigated, which correspond to FCB walls and CSEB panels for which well-documented experimental results are available in the literature. The FE responses of the different SMMs considered in this study are compared with experimental results in terms of predicted load-displacement response, strength, initial stiffness, collapse mechanism, computational efficiency, and output information.

2. Research Novelty and Significance

This paper fills several gaps in knowledge with regard to the use of SMMs to model the inelastic response behavior of unreinforced masonry walls. In particular, this study investigates the FE modeling of unreinforced masonry walls that do not satisfy the basic hypothesis of inelastic behavior concentrated at known locations by providing useful information for: (1) selecting constitutive models, FE solvers, and mesh discretization; (2) identifying under which conditions different SMMs can be used; and (3) suggesting potential development directions for more accurate, robust, and computationally efficient FE models of unreinforced masonry walls. To the authors' knowledge, this paper also represents the first rigorous investigation of the performance (in terms of accuracy and computational cost) of different SMMs in modeling the inelastic response of earth block masonry, which also acknowledges and identifies the inherent limitations of SMM approaches applied to earth block construction.

The present study aims to advance the FE modeling of unreinforced masonry with masonry units and masonry joints of similar mechanical properties, e.g., earth block masonry. Although this type of masonry is currently uncommon among new constructions, it is representative of many constructions with important historical value [54] and has the potential to expand into a significant portion of new low-rise buildings because of its sustainability, affordability, and safety advantages over other ordinary industrial construction materials [55–57].

3. Existing Simplified Micro-Modeling Techniques

The typical FE discretization of an unreinforced masonry wall using SMMs is shown in Fig. 1. In general, the masonry joint and potential crack interfaces are represented by zero-thickness interface elements, the response of which is described by a relation between the traction vector, $\boldsymbol{\sigma} = \{\sigma, \tau_s, \tau_t\}^T$, and the relative displacement vector, $\boldsymbol{u} = \{u_n, u_s, u_t\}^T$, in which σ is the normal stress, τ_s is the in-plane shear stress, τ_t is the out-of-plane shear stresses, u_n is the normal displacement, u_s is the in-plane relative shear displacement, and u_t is the out-of-plane relative shear displacement [5]. By contrast, the expanded masonry units are modeled using continuum FE elements, the mechanical behavior of which can be described by different material constitutive models, i.e., rigid, elastic, and inelastic constitutive models, corresponding to SMM-I, SMM-II, and SMM-III, respectively.

In order to accurately model the masonry's local and global mechanical behavior, SMMs need to account for all major failure mechanisms of masonry under multi-axial stress conditions [58–66], i.e.: (a) masonry crushing, (b) diagonal tension cracking of masonry units, (c) cracking of masonry joints, (d) failure of masonry joints due to sliding under combined normal and shear stress, and (e) cracking of masonry units in direct tension. In

SMM-I and SMM-II, all failure mechanisms are modeled through the constitutive model of the interface elements used to describe the masonry joint and potential crack interfaces. In particular, failure mechanisms (a) through (d), i.e., crushing, unit diagonal cracking, joint cracking, and joint sliding, are modeled via the masonry joint interface elements, and failure mechanism (e), i.e., unit tensile cracking, is modeled via the potential crack interface elements. In SMM-III, failure mechanism (a), i.e., crushing, is modeled via the expanded masonry unit elements, failure mechanisms (b) through (d), i.e., unit diagonal cracking, joint cracking, and joint sliding, are modeled via the masonry joint interface elements, and failure mechanism (e), i.e., unit tensile cracking, is modeled via the potential crack interface elements. SMM-I also requires the addition of an auxiliary interface element between the rigid expanded masonry units and the interface elements to ensure compatibility under large relative displacements among the rigid components [31].
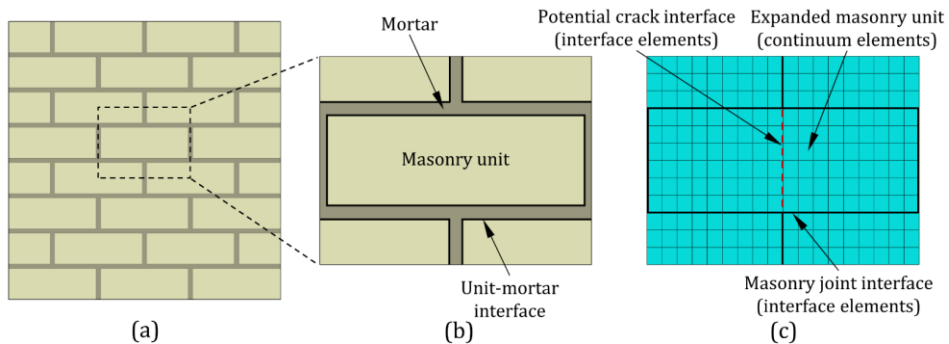

Fig. 1 Simplified micro-modeling techniques for unreinforced masonry: (a) masonry wall, (b) representative volume element of masonry, and (c) SMM representation.

In this paper, the capabilities and limitations of different SMMs were investigated using two benchmark examples representative of FCB and CSEB masonry, for which the SMMs were built using ABAQUS 6.14 [67], which is a general-purpose multi-physics commercial FE software widely used for unreinforced masonry modeling and simulation [3,5,12,31,46]. The accuracy, robustness, and computational efficiency of the different SMMs in simulating the structural response of masonry rely upon: (1) the material constitutive models used for the interface and expanded masonry unit element; (2) the FE solver; and (3) the FE mesh discretization. The selection of material constitutive models, FE solvers, and FE mesh discretization is discussed in the following sections.

3.1. Nonlinear Material Constitutive Models

SMMs employ nonlinear constitutive models for the interface elements corresponding to the masonry joint and potential crack interfaces in all SMMs and for the expanded masonry units in SMM-III. For SMM-I and SMM-II, rigid and elastic constitutive model, respectively, are used for the expanded masonry units. In this study, the recently developed coupled tension-shear interface model (CTSIM) [5] is employed for the interface elements, whereas the concrete damaged plasticity model (CDPM) [68,69] is used for the expanded masonry units in SMM-III.

The CTSIM is based on a convex composite failure surface comprising a tension-shear and a compression cap failure criterion [5], and requires the following input parameters: tensile strength (f_t); initial cohesion (C_0); apparent initial cohesion (C_{Q0}); initial friction angle (ϕ_0); residual friction angle (ϕ_r); initial dilatancy angle (ψ_0); residual dilatancy angle (ψ_r); mode-I fracture energy (G_f^I); mode-II fracture energy (G_f^{II}); compressive

stress at proportional limit $(\bar{\sigma}_0)$; peak compressive stress $(\bar{\sigma}_p)$; intermediate compressive stress corresponding to the inflection point in the softening branch $(\bar{\sigma}_m)$; residual compressive yield stresses $(\bar{\sigma}_r)$; plastic strain at peak compressive stress (κ_p); total plastic strain at intermediate compressive stress (κ_m); and parameter that controls the width of the compression cap failure surface in the shear stress axis (C_{ss}). These input parameters are derived from the experimental testing of: (1) masonry couplet specimens under uniaxial tensile loading, which provide f_t and G_f^I [53,70]; (2) masonry triplet specimens subjected to direct shear test with different pre-compression loads, which provide C_0, C_{Q0}, ϕ_0, ϕ_r, ψ_0, ψ_r and G_f^{II} [53,58–60]; (3) masonry prism or wallette specimens subjected to compression load, which provide $\bar{\sigma}_0$, $\bar{\sigma}_p$, $\bar{\sigma}_m$, $\bar{\sigma}_r$, κ_p, and κ_m [53,71,73]; and (4) masonry wallettes subjected to biaxial compression loads, which provide C_{ss} [62,63]. The compression cap failure criterion in the CTSIM can be easily disabled to better simulate the behavior of the potential crack interfaces, which cannot fail in compression in SMMs. Thus, when used in potential crack interfaces, the CSTIM requires only the following input parameters: f_t, C_0, C_{Q0}, ϕ_0, ϕ_r, ψ_0, ψ_r, G_f^I, and G_f^{II}. Of these parameters, f_t and G_f^I are obtained from a tensile test of masonry units [72]; $\tan\phi_0$, $\tan\phi_r$, $\tan\psi_0$ and $\tan\psi_r$ are assumed equal to 1; and other parameters (C_0, C_{Q0}, and G_f^{II}) are defined as function of f_t and/or G_f^I [4,5].

The CDPM is a continuum, plasticity-based, damage model for concrete and other quasi-brittle materials such as rocks, mortar, bricks, and ceramics [68,69]. This model requires the following input parameters: compressive stress-plastic strain curve, tensile stress-plastic strain curve, dilation angle (ψ_c), eccentricity (e_c), ratio of bi-axial compressive strength and uniaxial compressive strength (β_{bc}), ratio of the second stress invariant on the tensile meridian and on the compressive meridian (K_c), and viscosity parameter (η). These input parameters are derived from the experimental testing of: (1) masonry unit specimens under uniaxial tensile loading [72], which provide the tensile stress-plastic strain curve; (2) masonry prism or wallette subjected to compression load [53,71,73], which provide the compressive stress-plastic strain curve; and (3) masonry wallettes subjected to biaxial loads, which provide ψ_c, e_c, β_{bc}, and K_c [62,63,74]. Typically, the parameter η is obtained from calibration of the constitutive model to the experimental results used to obtain the other parameters [75].

3.2. FE Solver

The FE solver represents the set of algorithms used to solve the system on nonlinear equilibrium equations corresponding to a given FE model [67,76,77]. Three different families of FE solvers have been commonly used to simulate the nonlinear structural response of masonry structures: (1) implicit static FE solvers [6,28], (2) implicit dynamic FE solvers [78,79], and (3) explicit dynamic FE solvers [4,31,43]. The implicit static FE solvers are based on an iterative method (e.g., the Newton-Raphson method [76,80]) to solve the system of nonlinear equilibrium equations corresponding to a quasi-static loading (i.e., without inertial effects) applied incrementally. The implicit dynamic FE solvers use the same type of iterative algorithms for the system of nonlinear equilibrium equations as the implicit static FE solvers in conjunction with a time-stepping scheme that accounts for inertial forces, e.g., the Newmark-beta family of algorithms [76,81]. The

explicit dynamic FE solvers are based on an explicit integration algorithm (e.g., a central difference time integration or a predictor-corrector algorithm [82]) to extrapolate the nonlinear response of the structural model under consideration by using sufficiently small time increments to avoid instability (i.e., without using the equation of motion of the current time step to determine the current time step displacement) [67,77]. Implicit methods can be conditionally or unconditionally stable [67,76], whereas explicit methods are always conditionally stable with a maximum critical time step $\Delta t_{crit} = \min\left(L_e/C_d\right)$ [67,77], in which L_e denotes the characteristic length of any FE within the model, and C_d denotes the dilatational wave speed of the material in the given FE. In addition, static solvers can be used only for problems in which inertial effects can be neglected, whereas dynamic solvers can be used for problems in which inertial effects are significant or negligible. In fact, implicit static FE solvers used to simulate the mechanical behavior of masonry with SMMs could be affected by convergence issues due to the sudden release of elastic energy when cracks spread along the masonry joint interfaces and potential crack interface [4]. For these problems, dynamic FE solvers have been adopted to balance this sudden release of elastic energy through changes in the kinetic and viscous energy [4]. All three types of FE solvers are available in the FE software ABAQUS [67].

3.3. FE Discretization

A general SMM requires the full three-dimensional discretization of expanded masonry units and interface elements, which in general is very computationally demanding. The computational cost of three-dimensional SMMs can be reduced when the loads are applied in the plane of a wall by assuming a two-dimensional plane stress condition [20,28]. This assumption can provide accurate results for structures with single-wythe masonry walls and moderate levels of compressions [28,83]. When this assumption is not satisfied, a generalized or kinematic-enriched plane state can be used with good approximation for nonlinear analysis of masonry subjected to high levels of compressions [83,84].

A mesh sensitivity analysis must also be performed to ensure a good compromise between accuracy (i.e., convergence of FE response to a unique solution) and computational cost for a given SMM. For unconditionally stable implicit (static and dynamic) FE solvers, the mesh sensitivity analysis alone is sufficient to determine an acceptable FE mesh size [67]. However, for explicit dynamic FE solvers that are only conditionally stable, the maximum stable time step depends on both the mesh size and the material properties of the FE model. Therefore, the mesh sensitivity and the determination of the stable time step must be performed simultaneously for SMMs developed using explicit dynamic FE solvers. The identification of the coarser converged mesh and the corresponding maximum stable time step is needed to ensure the best compromise between accuracy, computational costs, and stability of the FE model.

In the investigation presented in this paper, plane stress conditions were assumed for all the SMMs because the two benchmark examples considered in this study (i.e., FCB and CSEB masonry walls) were single-wythe walls and these walls were not subjected to extreme compression stress. Therefore, the two-dimensional plane stress assumption can provide reasonably accurate results while considerably reducing the computational cost [28].

4. Performance Comparison of FE Response Analyses Using SMMs

The performance of different SMMs can be expressed in terms of the comparison between the experimentally-measured and numerically-estimated force-displacement responses, deformed shapes, stress distributions, and strain distributions. Often, a few global response parameters such as peak strength and initial stiffness are sufficient for design

purposes; however, these parameters need to be integrated at least with the information regarding the failure mode identified by the FE model. In this study, the FE response are compared with the experimental results by estimating the following point-wise relative error in the peak load $(P_{\max})$, initial stiffness (k), and displacement at failure (Δ_f):

$$\varepsilon_X = \frac{X_{\text{FE}} - X_{\text{exp}}}{X_{\text{exp}}} \tag{1}$$

where $X_{\text{FE}} = P_{\max}$, k, or Δ_f obtained from a FE analysis. When multiple nominally-identical replicas are experimentally tested, X_{exp} is taken as the average of the corresponding experimentally-measured values. In this study, the initial stiffness is defined as the secant stiffness evaluated at 1/10 of the average experimentally-measured peak load. Furthermore, the accuracy of the different FE models in estimating the force-displacement response curve is evaluated using three different global relative errors, i.e., the mean error $(\varepsilon_{\text{mean}})$, root mean squared error $(\varepsilon_{\text{RMS}})$, and mean absolute error $(\varepsilon_{\text{abs}})$, which are defined as follows:

$$\varepsilon_{\text{mean}} = \frac{1}{n_s} \sum_{j=1}^{n_s} \left[\frac{1}{n_j} \sum_{i=1}^{n_j} \frac{\left(P_{\text{FE}}^{(i)} - P_{\text{exp},j}^{(i)} \right)}{P_{\text{exp},j}^{(i)}} \right] \tag{2}$$

$$\varepsilon_{\text{RMS}} = \frac{1}{n_s} \sum_{j=1}^{n_s} \left[\sqrt{\frac{1}{n_j} \sum_{i=1}^{n_j} \left[\frac{P_{\text{FE}}^{(i)} - P_{\text{exp},j}^{(i)}}{P_{\text{exp},j}^{(i)}} \right]^2} \right] \tag{3}$$

$$\varepsilon_{\text{abs}} = \frac{1}{n_s} \sum_{j=1}^{n_s} \left[\frac{1}{n_j} \sum_{i=1}^{n_j} \frac{\left| P_{\text{FE}}^{(i)} - P_{\text{exp},j}^{(i)} \right|}{P_{\text{exp},j}^{(i)}} \right] \tag{4}$$

in which $P_{\text{exp},j}^{(i)}$ and $P_{\text{FE}}^{(i)}$ denote the experimentally-measured and numerically-simulated values, respectively, of the reaction force for a given masonry wall measured at a given level of displacement, $\Delta^{(i)}$; n_j denotes the number of recorded displacement levels for the *j*-th experimental sample, in which the maximum displacement level corresponding to the experimental displacement at failure; and n_s denotes the number of experimental specimens.

Another comparison criterion is provided by the computational efficiency of FE models with similar accuracy in reproducing the experimental behavior of masonry. The computational efficiency of different SMMs is expressed hereinafter in terms of computational time ratio (CTR), which is defined as the ratio of the computational CPU time corresponding to two different models and obtained using the same computer for a given FE response simulation.

5. Benchmark Example #1: Fired-Clay Brick (FCB) Masonry

The first benchmark example considered in this study consists of a series of FCB masonry shear walls, tested by Vermeltfoort and Raijmakers [85,86], in which the masonry units are considerably stronger than the mortar and the unit-mortar interfaces. For this type of

masonry, most of the inelastic behavior is expected to be concentrated at the masonry joints.

5.1. Description of Experimental Tests

The masonry shear walls considered in this example had a width-to-height ratio approximately equal to one, with dimensions 990 mm (length) × 1000 mm (height) × 100 mm (thickness). The walls were single-wythe walls consisting of 18 courses, with the bottom and top courses clamped to steel beams, as shown in Fig. 2(a). The masonry shear walls comprised wire-cut solid clay bricks with dimensions of 210 mm × 52 mm × 100 mm, and mortar layers of thickness equal to 10 mm. The experimental test involved a uniformly distributed normal pressure (p) applied vertically at the top of the walls, followed by a monotonically increasing horizontal displacement (Δ_H) applied to the top steel beam, while the bottom boundary was fixed.
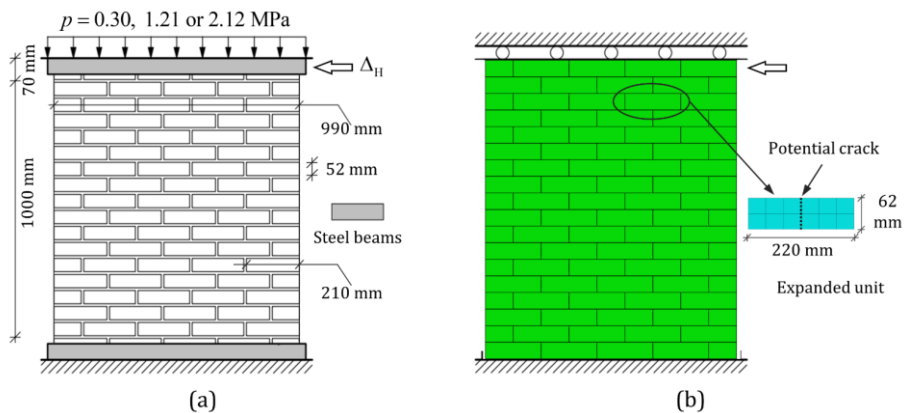
Fig. 2 FCB masonry: (a) shear walls and (b) SMM discretization of the shear wall.
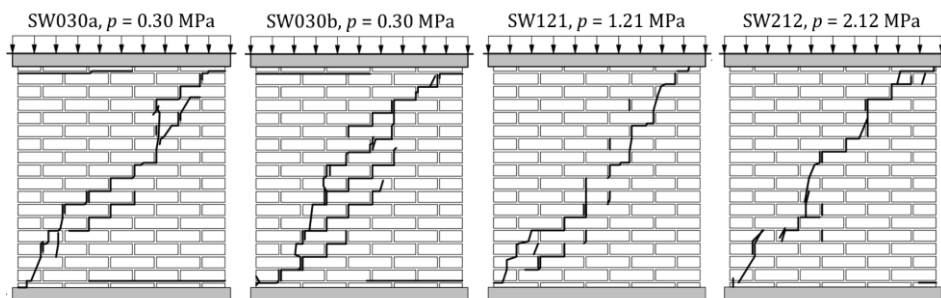
Fig. 3 Experimental crack patterns of the different FCB unreinforced masonry shear walls.

The FCB unreinforced masonry shear walls were experimentally tested for three different vertical pressures, i.e., wall SW030 (with two specimens SW030a and SW030b) was subjected to a constant pressure equal to 0.30 MPa, wall SW121 to a constant pressure equal to 1.21 MPa, and wall SW212 to a constant pressure equal to 2.12 MPa. The experimental failure patterns for the different walls are shown in Fig. 3. All the walls exhibited very similar experimental failure mechanisms and as expected, most of the cracking and inelastic behavior was concentrated at the masonry joints. During the

application of the monotonically increasing horizontal displacement, horizontal tensile cracks developed first at the bottom and top of the wall in the bed joints at earlier loading stages and were followed by diagonal stepped cracks. Finally, the crushing of the toes of the masonry and the tensile cracking in the middle of some masonry units led to the overall failure of each shear wall.

5.2. Description of SMMs Developed for the FCB Unreinforced Masonry

Fig. 2 (b) shows the SMM discretization of the FCB unreinforced masonry shear walls. The FE models were constructed using two-dimensional elements under the assumption of plane stress. The masonry joints and potential cracks interface were modeled by using a 4-node two-dimensional cohesive element, i.e., the COH2D4 element in ABAQUS 6.14 [67], and the expanded masonry units (having dimensions 220 mm × 62 mm) were modeled using a 4-node bilinear plane stress quadrilateral element with reduced integration and hourglass control, i.e., the CPS4R element in ABAQUS 6.14 [67]. Auxiliary interface elements were not needed in the SMM-I because the shear deformations in the masonry joints and potential crack interfaces were sufficiently small [31].

The material properties used for developing different SMMs were obtained from existing experimental results on tension, shear, and compression tests available in the literature [85,86]. An elastic modulus E_b =16,700 MPa and a Poisson ratio v_b = 0.15 were used for the expanded masonry units in SMM-II and SMM-III. The elastic and inelastic properties of the masonry joint interface for the different SMMs are given in Table 1, where k_n^b and k_s^b denote the normal and shear stiffness, respectively, of the masonry joint interfaces corresponding to the bed masonry joints; and k_n^h and k_s^h denote the normal and shear stiffness, respectively, of the masonry joint interfaces corresponding to the head masonry joints. The compressive input parameters given in the Table 1, i.e., $\bar{\sigma}_0$, $\bar{\sigma}_p$, $\bar{\sigma}_m$, $\bar{\sigma}_r$, κ_p and κ_m, were used to describe the stress-strain curve for the expanded masonry units in SMM-III based on a hardening/softening constitutive law used for the compression cap failure criterion of the CTSIM [5]. The values of the other parameters needed to fully define the CDPM for the expanded masonry units in the SMM-III were taken from the literature [74,75,87] and are: ψ_c = 38°, e_c = 0.1, β_{bc} = 1.16, K_c = 0.67, $\eta = 8.5 \times 10^{-5}$. The properties of potential crack interfaces used in the different SMMs are given in Table 2, where k_n and k_s are the normal and shear stiffness, respectively, of the potential crack interfaces.

5.3. Selection of FE Solver and Mesh Size

The implicit static, implicit dynamic, and explicit dynamic FE solvers, which are available in the FE software ABAQUS [67], were compared in terms of accuracy and computational effort for the SMM-IIs of the FCB masonry shear wall SW030. In the FE model based on the implicit static solver, all the degrees of freedoms were restrained at all the nodes at the top edge of the model, and a monotonically increasing horizontal displacement was applied on the side of the top course of the FE model while keeping the top edge of the FE model vertically fixed. A general procedure for static loading based on an incremental-iterative globally convergent Newton-Raphson method with the line search technique was used in ABAQUS [67]. In addition, an automatic load step increment technique was adopted for efficient and robust simulation of the response of the different FE models with initial, minimum, and maximum normalized increment sizes equal to 1×10^{-4}, 1×10^{-9}, 5×10^{-4}, respectively. In the FE model based on the implicit dynamic and explicit dynamic FE solvers, all the degrees of freedoms were restrained at the bottom edge of the model, and a fixed value of velocity V = 0.1 mm/s was applied at all nodes of the top edge of the wall. In addition, zero acceleration was assigned to the top edge of the model during the analysis

to ensure a linear variation with time of the top wall displacements. A density $\rho_b = 1.9 \times 10^3$ kg/m³ and mass-proportional damping, corresponding to a damping ratio $\zeta = 5\%$, were used for the solid elements to represent inertia and damping effects. For the implicit dynamic FE solver, a general implicit dynamic procedure was used, which was based on an incremental-iterative version of the globally convergent Newton-Raphson method [67] and an automatic load step increment having minimum normalized increment sizes equal to 5×10^{-4}. For the explicit dynamic FE solver, an explicit dynamic procedure based on the central-difference time integration was employed, with the critical time step equal to 3.3×10^{-6} s. The FE simulations were performed by increasing the applied displacement until the FE models became numerically unstable (i.e., due to collapse of the shear wall) or reached a 5.0 mm displacement at the top of the wall.

Table 1. Properties of masonry joint interfaces (SMM-I, SMM-II, and SMM-III) and inelastic compressive properties for the expanded masonry units (SMM-III) of the FCB unreinforced masonry shear walls.

Properties		SMM-I			SMM-II			SMM-III		
		SW030	SW121	SW212	SW030	SW121	SW212	SW030	SW121	SW212
k_n^b	(N/mm³)	62.9	78.1	62.9	82	110	82	82	110	82
k_s^b	(N/mm³)	27.6	35.5	27.6	36	50	110	36	50	110
k_n^h	(N/mm³)	39.4	63.8	39.4	82	110	82	82	110	82
k_s^h	(N/mm³)	17.3	29.0	17.3	36	50	110	36	50	110
f_t	(MPa)	0.250	0.160	0.160	0.250	0.160	0.160	0.250	0.160	0.160
C_0	(MPa)	0.362	0.232	0.232	0.362	0.232	0.232	0.362	0.232	0.232
C_{Q0}	(MPa)	18.125	11.6	11.6	18.125	11.6	11.6	18.125	11.6	11.6
$\tan\phi_0$	(-)	0.75	0.75	0.75	0.75	0.75	0.75	0.75	0.75	0.75
$\tan\phi_r$	(-)	0.75	0.75	0.75	0.75	0.75	0.75	0.75	0.75	0.75
$\tan\psi_0$	(-)	0.001	0.001	0.001	0.001	0.001	0.001	0.001	0.001	0.001
$\tan\psi_r$	(-)	0.0001	0.0001	0.0001	0.0001	0.0001	0.0001	0.0001	0.0001	0.0001
G_f^I	(N/mm)	0.018	0.012	0.012	0.018	0.012	0.012	0.018	0.012	0.012
G_f^{II}	(N/mm)	0.125	0.050	0.050	0.125	0.050	0.050	0.125	0.050	0.050
$\bar{\sigma}_0$	(MPa)	3.50	3.83	3.83	3.50	3.83	3.83	_3.50_	_3.83_	_3.83_
$\bar{\sigma}_p$	(MPa)	10.50	11.50	11.50	10.50	11.50	11.50	_10.50_	_11.50_	_11.50_
$\bar{\sigma}_m$	(MPa)	5.25	5.75	5.75	5.25	5.75	5.75	_5.25_	_5.75_	_5.75_
$\bar{\sigma}_r$	(MPa)	1.50	1.64	1.64	1.50	1.64	1.64	_1.50_	_1.64_	_1.64_
κ_p	(-)	0.090	0.090	0.090	0.090	0.090	0.090	_0.007_	_0.007_	_0.007_
κ_m	(-)	0.490	0.490	0.490	0.490	0.490	0.490	_0.033_	_0.033_	_0.033_
C_{ss}	(-)	9.0	9.0	9.0	9.0	9.0	9.0	-	-	-

Note: underlined values are for expanded masonry units of SMM-III.

Fig. 4 shows the experimental and numerical load-displacement responses and the CTR of the SMM-II corresponding to the different FE solvers and same mesh discretization. The CPU time for the explicit dynamic solver is used as reference (i.e., CTR = 1.0). Table 3 reports the different error estimates. All the FE solvers were able to simulate the behavior of the FCB masonry shear wall SW030 up to failure, and the FE load-displacement responses corresponding to the different solvers are similar. The value of ε_{RMS} and ε_{abs} for the different FE solvers are almost identical, varying between 8.22% and 8.61%

(approximately a 5.0% variation) and between 6.19% and 6.79% (approximately a 9.0% variation), respectively. The ε_{mean} values indicate that all solvers have a similar level of accuracy and slightly underestimate the FE response of the masonry wall, i.e., by 1.42%, 3.17% and 3.67% corresponding to implicit static, implicit dynamic, and explicit dynamic FE solvers, respectively. Also, the $\varepsilon_{P_{max}}$ and ε_k corresponding to the different FE solvers are small, i.e., less than 4.0% and 6.0%, respectively, showing that the different FE solvers can very accurately predict the peak load, P_{max}, and initial stiffness, k, of FBC masonry walls. By contrast, the ε_{Δ_f} is equal to 26.66%, 10.34%, and 15.43% for implicit static, implicit dynamic, and explicit dynamic FE solvers, respectively, which indicates that all FE solvers tend to overestimate the ultimate displacement of the masonry walls. This observation is not surprising, as it is known that the prediction of the structural response of unreinforced masonry walls after the peak strength has been reached is a very complex problem affected by significant uncertainties [88,89]. However, this discrepancy between experimental and numerical estimates of the displacement at failure could also be due to the fact that the criterion used to terminate the physical experiments is unknown (e.g., the experiments may have been interrupted before the complete collapse of the walls in order to protect the laboratory equipment); thus, the numerical results relative to the displacements at failure may or may not be representative of the experimental results. In Fig. 4(b), the comparison of the different CTRs shows that the explicit dynamic solver is the most computationally efficient solver among those considered in this study, as it produces FE analysis results 5.62 and 34.76 times faster than the implicit static and implicit dynamic FE solver, respectively. Based on these results, the explicit dynamic solver seems to provide the best compromise between accuracy and computational cost in simulating the behavior of masonry among the three FE solvers considered in this study.

Table 2. Properties of potential crack interfaces used in the SMMs of the FCB unreinforced masonry shear walls.

FE Model	k_n	k_s	f_t	C_0 / C_{Q0}	$\tan\phi_0 / \tan\phi_r$	$\tan\psi_0 / \tan\psi_r$	G_f^I / G_f^{II}
(-)	(N/mm³)	(N/mm³)	(MPa)	(MPa)	(-)	(-)	(N/mm)
SMM-I	159	69	2.0	2.9/2.9	1.0/1.0	1.0/1.0	0.008/0.5
SMM-II	16700	7260	2.0	2.9/2.9	1.0/1.0	1.0/1.0	0.008/0.5
SMM-III	16700	7260	2.0	2.9/2.9	1.0/1.0	1.0/1.0	0.008/0.5

Table 3. FE results of the FCB unreinforced masonry shear walls in term of errors between the experimental and FE load-displacement curve corresponding to different FE solvers.

FE Solver	$\varepsilon_{P_{max}}$	ε_k	ε_{Δ_f}	ε_{mean}	ε_{RMS}	ε_{abs}
(-)	(%)	(%)	(%)	(%)	(%)	(%)
Implicit Static	1.89	3.05	26.66	-1.42	8.48	6.45
Implicit Dynamic	3.82	5.99	10.34	-3.17	8.22	6.19
Explicit Dynamic	0.31	4.01	15.43	-3.67	8.61	6.79

A mesh sensitivity analysis of the FE SMM-II model of masonry shear wall SW030 was performed. The FE models were analyzed by using the explicit dynamic FE solver and a maximum time increment equal to the critical time step. It was found that the critical time step of the SMMs depends only on the thickness of the interface elements, and the mesh size of the expanded masonry units does not affect the critical time step for any practical FE discretization. Thus, the thickness of the interface elements was set equal to 0.05 mm, giving a critical time step equal to 3.3×10^{-6} s, and the mesh sensitivity analysis was performed by developing SMM-IIs with four different mesh sizes for the expanded

masonry units of the FCB masonry shear wall SW030. These meshes are identified by two numbers representing the number of elements used along the length and height of the expanded masonry units, respectively. The mesh sensitivity analysis was performed starting from a coarse 6×2 mesh, and progressively increasing the number of elements in each direction in a proportional manner until convergence was achieved. Convergence was verified by calculating the point-wise changes in peak load $\left(\delta_{P_{\max}}\right)$, initial stiffness $\left(\delta_k\right)$, and displacement at failure $\left(\delta_{\Delta_f}\right)$, defined as:

$$\delta_X = \frac{X_{m2} - X_{m1}}{X_{m1}} \tag{5}$$

in which X_{m_1} and $X_{m_2} = P_{\max}$, k, or Δ_f obtained from the FE analysis corresponding to the two mesh discretization being compared; as well as the global relative difference $\left(\delta_{abs}\right)$, which is defined as:

$$\delta_{abs} = \frac{1}{n_m} \sum_{i=1}^{n_m} \frac{\left|P_{m_2}^{(i)} - P_{m_1}^{(i)}\right|}{P_{m_1}^{(i)}} \tag{6}$$

in which $P_{m_1}^{(i)}$ and $P_{m_2}^{(i)}$ denote the reaction forces at displacement $\Delta^{(i)}$ obtained from the FE analysis corresponding to the two mesh discretization being compared; and n_m denotes the minimum of the number of displacement levels before failure for the two meshes being compared. In particular, it was assumed the convergence was achieved when the four convergence measures reached an absolute value smaller than 1%. The following meshes were developed: 6×2, 12×4, 18×6, and 24×8. The horizontal load-displacement responses of the considered SMM-IIs are shown in Fig. 5(a), and the corresponding CTRs are compared in Fig. 5(b), in which mesh 18×6 is used as reference. It is observed that the FE load-displacement curves corresponding to meshes 18×6 and 24×8 are almost overlapped, whereas the other meshes provide significantly different response results. In addition, it is observed that the computational cost increases by a factor approximately equal to 3 going from one mesh size to the next finer mesh.
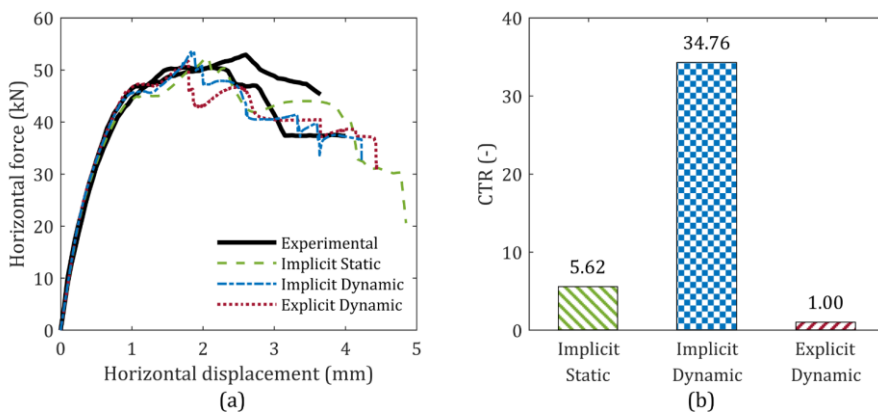

Fig. 4 FE results corresponding to different FE solvers: (a) comparison of experimental and FE load-displacement curves, and (b) comparison of CTR for different FE solvers.

The values of the convergence measures are reported in Table 4. As expected, the convergence measures rapidly decrease in absolute value when refining the mesh, and they are all smaller than 1% in absolute value going from mesh 18×6 to mesh 24×8, which indicates that convergence has been achieved. Based on the results obtained in this mesh convergence analysis, mesh 18×6 was used for SMM-II and SMM-III hereinafter in conjunction with the FE explicit dynamic solver and a maximum time increment equal to 3.3 × 10-6 s.
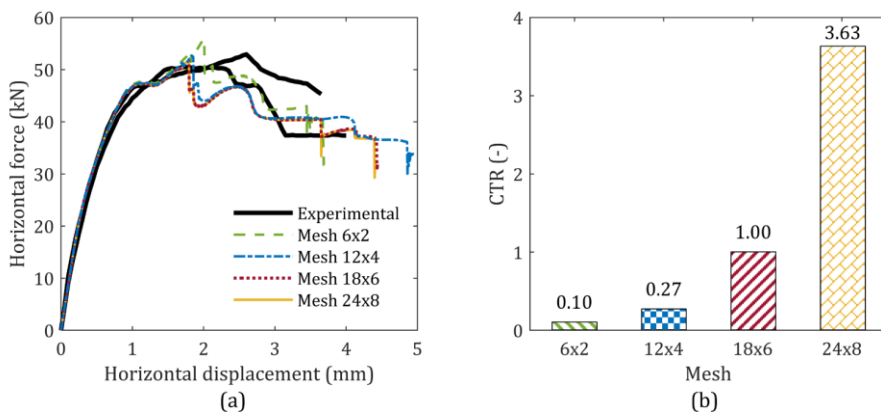

Fig. 5 Comparison of different mesh discretization for the SMM-IIs: (a) load-displacement curves, and (b) CTRs with mesh 18x6 as reference mesh.

Table 4 FE response of the SMM-IIs corresponding to the four different meshes in term of relative difference among the FE load-displacement curve.

Mesh		$\delta_{P_{max}}$	δ_k	δ_{Δ_f}	δ_{abs}
m_1	m_2	(%)	(%)	(%)	(%)
6×2	12×4	-4.60	-0.39	34.15	3.27
12×4	18×6	-1.95	-0.22	-10.30	1.54
18×6	24×8	-0.01	-0.01	-0.68	0.21

5.4. Comparison of the FE Results Obtained Using Different SMMs

The FE results corresponding to the different SMMs of the FCB unreinforced masonry shear wall having different initial pressure, i.e., SW030, SW121, and SW212 are presented in Fig. 6(a-c) compares the experimentally-measured horizontal force-horizontal displacement response of the shear walls with the corresponding numerically-estimated FE responses of the different SMMs considered in this investigation. The sudden load drops in the FE force-displacement responses are due to cracking of expanded masonry units at the potential crack locations. The FE results show that all SMMs can reproduce the complete load path of the FCB unreinforced masonry shear wall up to and beyond the peak strength. Fig. 6(d) presents the CTRs corresponding to different FE models. All the FE simulations for the SMMs of the FCB unreinforced masonry shear wall were run on a Microsoft Windows-based personal computer having an Intel(R) Core (TM) i7-8700 CPU @ 3.19 GHz with 16.0 GB RAM, with only one CPU core used in each simulation. The CPU time for the SMM-II is used as reference (i.e., CTR = 1.0) for each FCB unreinforced masonry shear wall. As expected, the results show that the computation demand is lowest for SMM-I and highest for SMM-III for all modeled shear walls.

The different error measures for all models are reported in Table 5. For the SW030 shear wall, SMM-II provides the most accurate predictions for the peak load and the initial stiffness, SMM-I provides the best prediction of the displacement at failure, and SMM-III presents the lowest global relative errors (i.e., $\varepsilon_{\text{mean}}$ = 2.58%, ε_{RMS} = 8.33%, and ε_{abs} = 6.42%), although these errors are very similar to those for SMM-II ($\varepsilon_{\text{mean}}$ = -3.67%, ε_{RMS} = 8.61%, and ε_{abs} = 6.79%), whereas they are significantly (approximately two to four times) higher for SMM-I. For the SW121 shear wall, SMM-I provides the most accurate estimate of P_{max} , SMM-II provides the most accurate estimate of k and Δ_{f} , and SMM-III has the lowest value for $\varepsilon_{\text{mean}}$, ε_{RMS} , and ε_{abs} , i.e., 1.32%, 4.15%, and 3.36%, respectively. For the SM212 shear wall, The SMM-II always provides the lowest errors between the experimental and numerical estimates, with the exception of $\varepsilon_{P_{\text{max}}}$, for which SMM-I gives the lowest value, i.e., $\varepsilon_{P_{\text{max}}}$ = 8.18%. SMM-I generally underestimate all response quantities for all walls considered in this study, with the exception of the peak strength of the SW212 wall, for which $\varepsilon_{P_{\text{max}}}$ = 8.18%. The SMM-I also presents the largest ε_k , $\varepsilon_{\text{mean}}$, ε_{RMS} , and ε_{abs} among all the SMMs, these errors increase in magnitude for increasing values of the initial vertical pressure applied to the shear wall. SMM-II always slightly overestimates the peak load (with 0.31% ≤ $\varepsilon_{P_{\text{max}}}$ ≤ 15.20%) and initial stiffness (with 1.59% ≤ ε_k ≤ 5.34%), with errors $\varepsilon_{P_{\text{max}}}$, $\varepsilon_{\text{mean}}$, ε_{RMS} , and ε_{abs} increasing in magnitude for increasing values of the initial vertical pressure applied to the shear wall. SMM-III presents largest error in Δ_{f} for all the shear walls (with 24.43% ≤ $\varepsilon_{\Delta_{\text{f}}}$ ≤ 26.71%), always overestimating the displacement at failure. However, SMM-III has also the lowest global relative errors for the SW030 and SW121 walls.

It is noted that the numerical value of $\varepsilon_{P_{\text{max}}}$ for all SMMs increases for increasing levels of initial vertical pressure, whereas this phenomenon is not observed for ε_k or $\varepsilon_{\Delta_{\text{f}}}$, for which no simple pattern can be identified. The magnitude of $\varepsilon_{P_{\text{max}}}$ also increasing for increasing initial vertical pressure for SMM-II and SMM-III, whereas it achieves a minimum value in correspondence to SW121 for SMM-I. This phenomenon is likely due to the use of a single vertical potential crack interface at a prescribed location, which provides a proper representation of the cracking pattern observed for walls with lower initial vertical pressure. However, for higher values of initial vertical pressure, the experimental cracking pattern show diagonal cracks in the masonry units, which cannot be properly represented by the vertical potential crack interfaces in the expanded masonry units of the SMMs.

The FE crack patterns and the distribution of the in-plane minimum principal stress for the SMMs of the FCB unreinforced masonry shear walls are presented in Fig. 7(a-c) for SMM-I, Fig. 7(d-f) for SMM-II, and Fig. 7(g-i) are for SMM-III. In order to make the cracks visible, the deformed shape in Fig. 7 is magnified by a factor 10. The numerically-simulated inelastic behavior of the shear wall is similar to the actual behavior observed in the experimental tests: horizontal tensile cracks start developing first at the bottom and top of the shear walls at approximately 1.0 mm of horizontal displacement, followed by a diagonal stepped crack in the shear wall. After approximately 2.5 mm of horizontal displacement, a combined shear and crushing mechanism develops at the toe of the shear wall, which leads to the failure of the model. All the different SMMs reproduce almost the same crack patterns for each of the walls, and these patterns are very similar to those observed experimentally. The distribution of the in-plane minimum principal stress in the SMM-II and SMM-III shows that small diagonal compressive struts, which pass through the center of the bricks, form in all SMMs when horizontal cracks develop at the bottom and top of the shear wall. With further increase in the displacement, the formation of additional

compressive struts is averted by the initiation of the diagonal crack in the SMMs. Finally, when the diagonal crack is fully open, two distinct struts are formed on each side of the diagonal crack, as shown in the Fig. 7. The compressive stress in the struts increases with increasing levels of initial vertical pressure, i.e., the compressive stress is lowest in the SW030 walls and highest in the SW212 walls. The maximum compressive stress values in the SMM-II for the SW030 and SW121 shear walls remain below 8.0 and 9.9 MPa, respectively, which indicates that the assumption of linear elastic behavior in the expanded masonry units is reasonable. In fact, the compressive strength of the masonry units is not available [6,46]; however, it can be estimated as approximately equal to 20 MPa. This estimate is based on the tensile strength, which is equal to 2.0 MPa, and the reasonable assumption of a ratio of compressive to tensile strength equal to 10 [46,90]. In SMM-III, the compressive stress values for the SW030 and SW121 shear walls are found to be slightly lower, i.e., approximately 7.5 and 9.4 MPa, respectively, than the corresponding compressive stress values in the SMM-II (i.e., 8.0 and 9.9 MPa, respectively), with a negligible plastic strain in the expanded masonry units, i.e., less than 1.0×10^{-4}. The maximum compressive stress in the SMM-II for the SW212 wall reaches approximately 13.9 MPa, which is closer to the compressive strength of the masonry units when compared to the maximum compressive stress values in the SMM-II for the SW030 and SW121 shear walls. In the SMM-III of the SW212 wall, the compressive stress is approximately equal to 12.5 MPa (which is achieved at a horizontal displacement of approximately 2.9 mm, when a drop in horizontal force is observed), and the plastic strain is approximately equal to 9.8×10^{-3}, indicating a significant plasticization of the expanded masonry units.
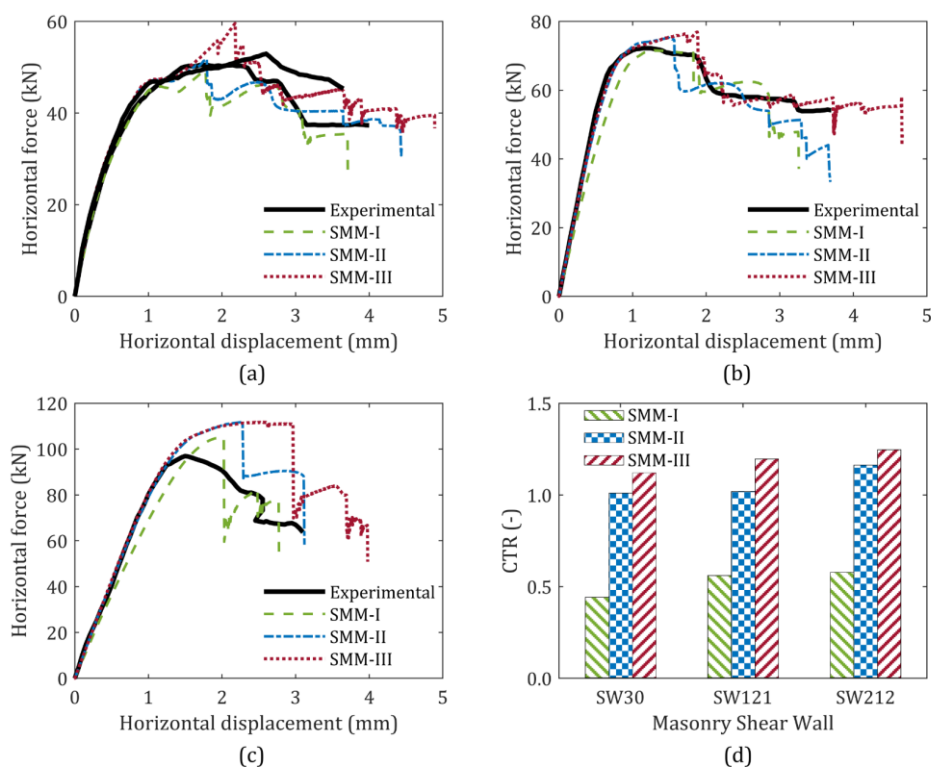

Fig. 6 Comparison of the experimentally-measured and numerically-simulated force-displacement response for the SMMs of the FCB unreinforced masonry shear walls: (a) SW030, (b) SW121, (c) SW212, and (d) CTR corresponding to different FE models.

Table 5. FE Simulation results for the SMMs of the FCB unreinforced masonry shear walls in term of errors between the experimental and FE load-displacement curve.

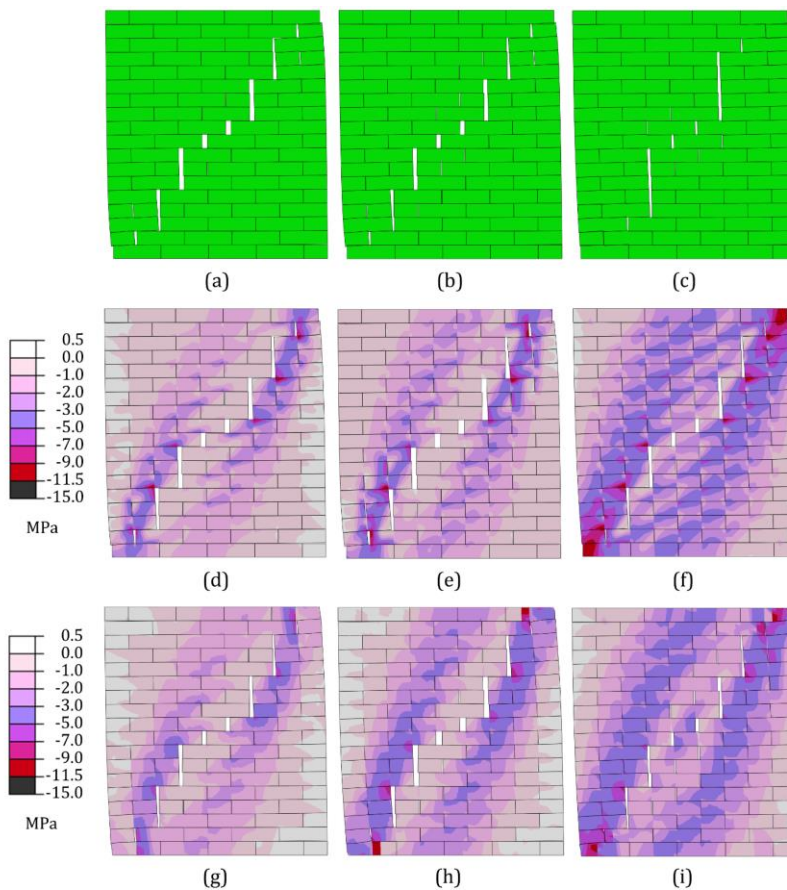| Shear Wall (-)	FE Modal (-)	$\varepsilon_{P_{max}}$ (%)	ε_k (%)	ε_{Δ_f} (%)	ε_{mean} (%)	ε_{RMS} (%)	ε_{abs} (%)
SW030	SMM-I	-4.08	-10.01	-3.24	-12.78	21.53	12.82
	SMM-II	0.31	4.01	15.43	-3.67	8.61	6.79
	SMM-III	14.95	5.13	27.71	2.58	8.33	6.42
SW121	SMM-I	-0.59	-10.56	-13.22	-17.02	35.31	19.48
	SMM-II	4.40	5.34	-2.27	-6.02	14.71	8.28
	SMM-III	6.70	6.29	24.43	1.32	4.15	3.36
SW212	SMM-I	8.18	-11.40	-11.49	-17.37	36.11	20.85
	SMM-II	15.20	1.59	-0.61	11.48	18.33	13.09
	SMM-III	15.26	1.80	26.86	16.70	28.23	18.96

Fig. 7 FE crack patterns and distribution of in-plane minimum principal stress for the SMMs of the FCB unreinforced masonry shear walls: (a-c) SW030, SW121 and SW212 for SMM-I; (d-f) SW030, SW121 and SW212 for SMM-II; and (g-i) SW030, SW121 and SW212 for SMM-III.

The level of information provided by the different models increases with the computational cost: SMM-I are associated with the lowest computational cost but also with the lowest level of information, which is limited to the global load and deformation level and the cracking pattern; SMM-III is the most computationally expensive models but provide information on stresses and strains in both elastic and plastic ranges within the expanded masonry units.

It is concluded that all three SMMs considered in this study can properly simulate the global horizontal load-displacement behavior of the FCB unreinforced masonry shear walls and can capture the experimentally observed failure mechanism of these walls, for which the inelastic behavior is concentrated along the mortar-unit interfaces and in potential cracks of known locations. However, the SMMs may not be able to properly predict the experimental displacement at failure, although this result may also depend on the lack of knowledge for the termination criterion used in the experimental tests. SMM-II and SMM-III present similar levels of accuracy and perform better than SMM-I in capturing the experimental behavior of the shear walls. However, their accuracy slightly degrades for increasing levels of initial vertical pressure applied to the walls.

6. Benchmark Example #2: Compressed and Stabilized Earth Block (CSEB) Masonry

The second application example considered in this study is a CSEB unreinforced masonry wallette, in which cracking and inelastic behavior is spread across the different components (i.e., masonry units, mortar, and unit-mortar interfaces) of the masonry walls.

6.1. Description of Experimental Tests

A diagonal compression test performed on three replicate CSEB masonry wallettes (Wall-1, Wall-2 and Wall-3), reported in [53], was selected for this investigation. Each specimen consisted of a single-leaf, eight-course CSEB masonry wallette having dimensions of 864 mm (length) × 787 mm (height) × 178 mm (thickness), as shown in Fig. 8(a). The specimens were built using: (1) CSEBs with dimensions equal to 254 mm × 178 mm × 89 mm and fabricated using silty loam soil and 6% cement; and (2) earthen mortar layers of thickness equal to 13 mm and fabricated using a cement:soil:sand proportion by weight equal to 1:1:6 and water-to-cement ratio equal to 2.4. The CSEB masonry wallettes were tested under diagonal compression force that was imparted through steel shoes that were placed at the top and bottom corner of each specimen, as illustrated in Fig. 8(a). The experimental test involved a monotonically increasing vertical displacement on the steel shoe at the top of the masonry wallettes, while keeping the boundaries of the steel shoe at bottom of the masonry wallette fixed. The horizontal extension and vertical contraction were recorded using two displacement transducers, which are labeled as "A" and "B", respectively, in Fig. 8(a).

Fig. 9 shows the experimental crack patterns of the three wallettes at the end of the diagonal compression test. The specimens exhibited consistent failure modes with diagonal cracks parallel to the direction of the load and inclined by approximately 45° with respect to the bed joints. As shown in Fig. 9, the cracks at failure were observed mainly through the CSEBs and to a lesser extent along the head and bed joints and affected in a minor manner the mortar joints. This behavior is common for CSEB masonry and is fundamentally different from that of ordinary masonry, in which specimens typically fail mostly along the bed and head joints.

6.2. Description of the SMMs for the CSEB Masonry Wallette

Fig. 8(b) presents a schematic of the FE models that were developed to simulate the response of the CSEB masonry wallettes. The models were constructed using the two-dimensional elements under the assumption of plane stress as those used for the FCB

masonry walls, i.e., the CPS4R and COH2D4 elements in ABAQUS 6.14 [67]. Also in this case, auxiliary interface elements were not used in SMM-I. All FE models were analyzed using the explicit dynamic FE solver with time step equal to the critical time step of 2.5×10^{-6} s. All degrees of freedoms at the bottom edge of the bottom steel shoe were fixed in the FE models, and a constant vertical velocity of $V = 0.1$ mm/s (i.e., with zero acceleration) was applied downward to the top edge of the top steel shoe. A density $\rho_b = 1.8 \times 10^3$ kg/m³ and mass-proportional damping corresponding to a damping ratio $\zeta = 5\%$ were used for the solid elements of the wall to model inertia and damping effects. Based on a mesh sensitivity analysis performed as described for the previous benchmark example, the mesh used for the SMMs of the CSEB masonry wallettes consisted of 12 interface elements employed for each bed joints (i.e., six interface elements for the bed joint of each half masonry unit), five interface elements for each head joint and for the potential vertical cracks, and 30 elements for each half of the expanded masonry units (having dimensions 267 mm × 102 mm). Each half of the expanded masonry units was represented by a rigid element for the SMM-I.

The steel shoes were modeled as linear elastic for all the SMMs, with a surface-based tie constraint [67] imposed between the masonry and the steel shoes. The steel shoes were modeled also using CPS4R elements [67], with elastic modulus $E_{steel} = 21,000$ MPa, Poisson ratio $\nu_{steel} = 0.30$, density $\rho_{steel} = 7.85 \times 10^3$ kg/m³, and damping ratio $\zeta_{steel} = 5\%$. The mesh of the steel shoes was extruded from the masonry wallettes in order to obtain a continuous mesh. The steel shoes were discretized using two elements in the direction orthogonal to that of the extrusion.
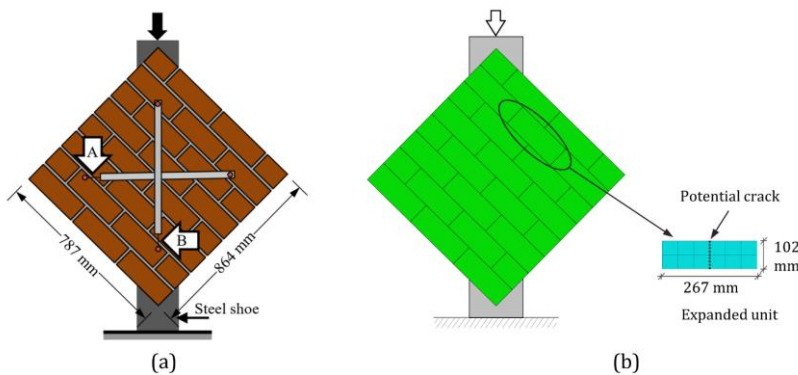

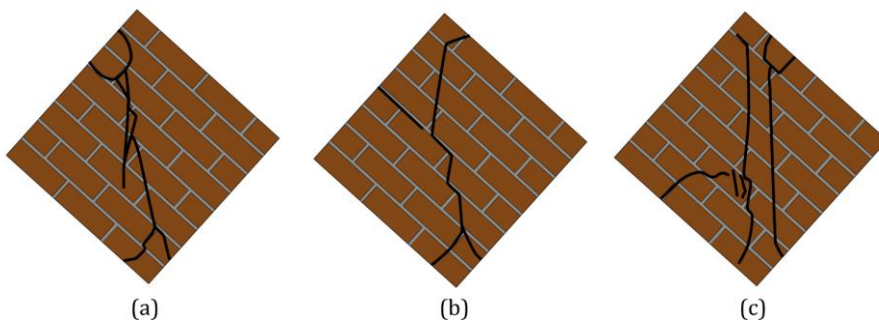Fig. 8 CSEB masonry wallette: (a) test setup and (b) SMM discretization.

Fig. 9 Experimental crack patterns of the CSEB masonry wallettes: (a) Wall-1, (b) Wall-2, and (c) Wall-3.

The material properties of the different components used in the SMMs were obtained from existing experimental results on tension, shear, and compression tests available in [53,91,92]. These experimental tests were performed on the same batch of CSEBs, and mortar used to build the CSEB masonry wallettes analyzed in this study. An elastic modulus E_b = 2550 MPa and a Poisson ratio v_b = 0.17 were used for the expanded masonry units in SMMs-II and SMM-III. The properties of the masonry joint and potential crack interface used in the different SMMs are given in Table 6, where k_n^b and k_s^b denote the normal and shear stiffness, respectively, of the masonry joint interfaces corresponding to the bed masonry joints; and k_n^h and k_s^h denote the normal and shear stiffness, respectively, of the masonry joint interfaces corresponding to the head masonry joints. For the potential crack interfaces, $k_n^b = k_n$ denote the normal stiffness, and $k_s^b = k_s$ denote the shear stiffness of the interface. Similar to the FCB unreinforced masonry shear wall, the input parameters given in the Table 6 were used to describe the stress-strain curve for the expanded masonry units in SMM-III based on a hardening/softening constitutive law used for the compression cap failure criterion of the CTSIM [5]. The other CDPM parameters used in the SMM-III are: ψ_c = 38°, e_c = 0.1, β_{bc} = 1.16, K_c = 0.67, η = 8.5×10^{-5} [91,92].

Table 6. Properties of masonry joint/potential crack interfaces (SMM-I, SMM-II, and SMM-III) and inelastic compressive properties for the expanded masonry units (SMM-III) of the CSEB masonry wallettes.

Properties		Masonry joint interface			Potential crack interface		
		SMM-I	SMM-II	SMM-III	SMM-I	SMM-II	SMM-III
k_n^b	(N/mm³)	24.38	907.10	907.10	159.00	2555.00	2555.00
k_s^b	(N/mm³)	10.44	429.67	429.67	69	1091.45	1091.45
k_n^h	(N/mm³)	17.89	907.10	907.10	-	-	-
k_s^h	(N/mm³)	7.66	429.67	429.67	-	-	-
f_t	(MPa)	0.146	0.146	0.146	0.510	0.510	0.510
C_0	(MPa)	0.290	0.290	0.290	0.714	0.714	0.714
C_{Q0}	(MPa)	29.000	29.000	29.000	0.714	0.714	0.714
$\tan\phi_0$	(-)	1.51	1.51	1.51	1.00	1.00	1.00
$\tan\phi_r$	(-)	1.51	1.51	1.51	1.00	1.00	1.00
$\tan\psi_0$	(-)	0.440	0.440	0.440	1.00	1.00	1.00
$\tan\psi_r$	(-)	0.044	0.044	0.044	1.00	1.00	1.00
G_f^I	(N/mm)	0.00212	0.00212	0.00212	0.0090	0.0090	0.0090
G_f^{II}	(N/mm)	0.02120	0.02120	0.02120	0.0495	0.0495	0.0495
$\bar{\sigma}_0$	(MPa)	1.29	1.29	<u>1.29</u>	-	-	-
$\bar{\sigma}_p$	(MPa)	3.88	3.88	<u>3.88</u>	-	-	-
$\bar{\sigma}_m$	(MPa)	1.94	1.94	<u>1.94</u>	-	-	-
$\bar{\sigma}_r$	(MPa)	0.55	0.55	<u>0.55</u>	-	-	-
κ_p	(-)	0.011	0.011	<u>0.011</u>	-	-	-
κ_m	(-)	0.044	0.044	<u>0.044</u>	-	-	-
C_{ss}	(-)	9.0	9.0	-	-	-	-

Note: underlined values are for expanded masonry units of SMM-III

6.3. FE Results

Fig. 10(a) compares the FE force-displacement responses obtained using the different SMMs considered in this investigation with the corresponding experimentally-measured response obtained from the diagonal compression test. Positive and negative displacements correspond to horizontal extension and vertical contraction, respectively, which were experimentally recorded using the displacement transducers A and B, as shown in the Fig. 10(a). Fig. 10(b) presents the CTRs corresponding to the different FE models, which shows that SMM-I is the least computationally demanding model, whereas SMM-III is the most computationally expensive one. The six error measures considered in this study and corresponding to the different SMMs are reported in Table 7. All SMMs significantly overestimate the peak axial force, $P_{\max}$, of the CSEB masonry wallettes, with errors $\varepsilon_{P_{\max}} = 129.85\%$, 68.44%, and 53.96% for SMM-I, SMM-II, and SMM-III, respectively. In addition, all FE models underestimate the initial stiffness, k, both in the horizontal direction, with ε_k varying between -44.20% (SMM-I) and -31.04% (SMM-II and SMM-III), and in the vertical direction, with ε_k varying between -25.71% (SMM-II and SMM-III) and -10.63% (SMM-I). SMM-I and SMM-III highly overestimate the displacements at failure in both horizontal (ε_{Δ_f} = 507.53% and 49.95%, respectively) and vertical (ε_{Δ_f} = 44.50% and 39.55%, respectively) directions. The errors are significantly smaller for the SMM-II, with ε_{Δ_f} = 1.80% and -6.96% in the horizontal and vertical directions, respectively. The discrepancies between the force-displacement responses are also larger than for the FCB masonry walls, as reported in Table 5. It is noteworthy that, given the definition of n_j in Eqs. (2) through (4), the global relative errors $\varepsilon_{\text{mean}}$, ε_{RMS}, and ε_{abs} are less meaningful when large discrepancies are observed between the experimental and numerical estimates of the displacement at failure, as it is the case here.

Table 7. Comparison of the FE simulation results for the CSEB masonry wallettes in term of errors between experimental and FE load-displacement curves.

Displacements (-)	FE Model (-)	$\varepsilon_{P_{\max}}$ (%)	ε_k (%)	ε_{Δ_f} (%)	$\varepsilon_{\text{mean}}$ (%)	ε_{RMS} (%)	ε_{abs} (%)
Horizontal extension	SMM-I	129.85	-44.20	507.53	-11.59	22.95	18.35
	SMM-II	68.44	-31.04	1.80	10.01	27.62	22.39
	SMM-III	53.96	-31.04	49.95	4.51	20.54	17.45
Vertical contraction	SMM-I	-	-10.63	44.50	53.09	59.24	54.45
	SMM-II	-	-25.71	-6.96	16.49	47.32	39.87
	SMM-III	-	-25.71	39.55	20.97	26.84	24.77

The crack patterns and distribution of in-plane minimum principal stress observed at 0.25mm displacement and the displacement at failure for the SMMs of the CSEB masonry wallettes are presented in Fig. 11(a) and (d) for SMM-I, Fig. 11(b) and (e) for SMM-II, and Fig. 11(c) and (f) for SMM-III. In order to make the cracks visible, the deformed shape in Fig. 11 is magnified by a factor 10. The FE crack patterns of the SMMs do not match the experimental crack patterns of the CSEB masonry wallettes shown in Fig. 11. In fact, the cracks simulated in all SMMs are mostly concentrated at the bottom two masonry bed joints and at the head joints and potential crack interfaces of the bottom two courses of the masonry wallette. As expected, the SMMs are unable to simulate the diagonal cracks observed experimentally in the earthen blocks and, thus, cannot capture the experimental failure mode of the CSEB masonry wallettes.
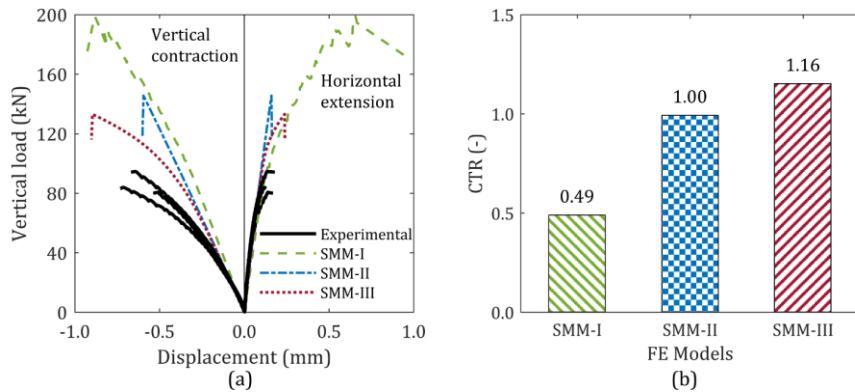
Fig. 10 FE results for the CSEB masonry wallettes: (a) comparison of the experimental and FE load-displacement responses, and (b) CTRs corresponding to different FE models.
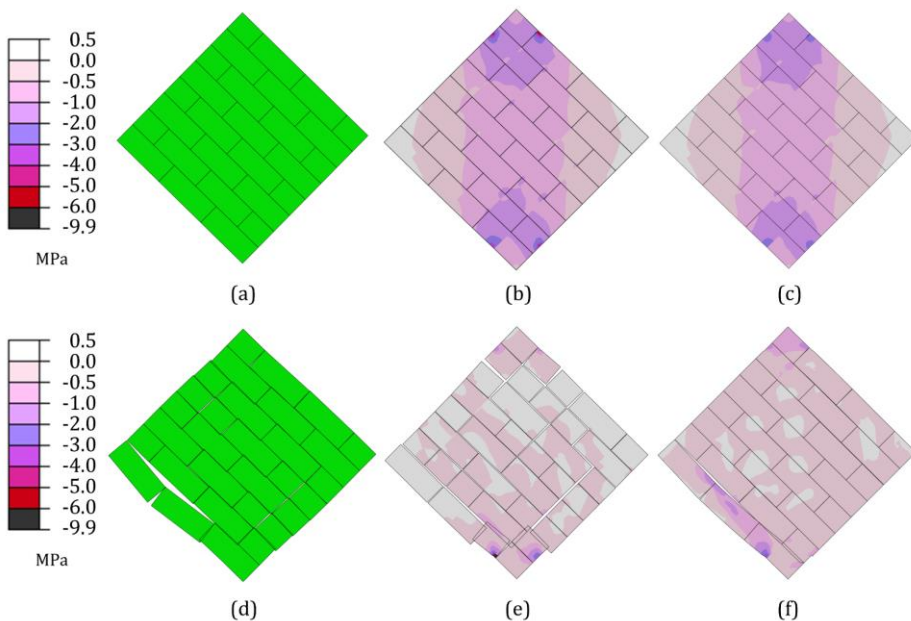

Fig. 11 FE crack patterns and distribution of in-plane minimum principal stress for the SMMs of the CSEB masonry wallettes: (a-c) SMM-I, SMM-II and SMM-III, respectively, at 0.25 mm displacement; and (d-f) SMM-I, SMM-II and SMM-III, respectively, at failure displacement.

It is concluded that the SMMs are unable to simulate the behavior of the CSEB masonry wallettes subjected to a diagonal compression test. This result is due to the fact that CSEB masonry does not satisfy the hypothesis that mortar and unit-mortar interfaces are significantly weaker than the masonry units, which is at the basis of the SMMs. In fact, the assumption that the inelastic behavior is concentrated along the masonry joints and the middle plane of the masonry units is not valid for CSEB masonry, where the experimental evidence shows cracking patterns that are similarly distributed across joints and masonry units. It is also concluded that a modeling approach different than SMM is needed to

properly describe the mechanical behavior of CSEB masonry walls with masonry units of similar strength and stiffness as the mortar and the unit-mortar interfaces. Such new modeling approach needs to be able to model the propagation of cracks with any inclination within the masonry units and the mortar.

5. Conclusions

In this study, the capabilities and limitations of FE simplified micro-modeling techniques were investigated through a comparative analysis of their simulation capabilities with respect to two different types of masonry, i.e., fired-clay brick (FCB) and compressed and stabilized earth block (CSEB) masonry. In the simplified micro-modeling technique, mortar and adjacent unit-mortar interfaces in the masonry are represented by zero-thickness interface elements between expanded masonry units, with a vertical potential crack interface placed in the middle of the expanded masonry units. Different simplified micro-models (SMMs) can be developed based on the different material constitutive models used for the masonry units. This study considered rigid (SMM-I), elastic (SMM-II), and elasto-plastic (SMM-III) constitutive models. The comparative analysis was made between experimentally-measured and numerically-simulated responses of benchmark unreinforced masonry walls that are representative of the two masonry types and for which well-documented experimental data are available in the literature.

This paper also provides recommendations on the use of different FE solvers and on the mesh and time step discretization for developing accurate and robust SMMs within the FE framework. In particular, it is shown that implicit static, implicit dynamic, and explicit dynamic solvers produce similar mechanical responses when used to simulate the nonlinear inelastic behavior of unreinforced masonry walls; however, the explicit dynamic solver is significantly more efficient than the other solvers from a computational point of view.

The FCB unreinforced masonry shear walls showed experimental inelastic behavior and cracks concentrated in the masonry joints (i.e., mortar and unit-mortar interfaces) and in potential crack zones corresponding to the vertical middle plane of the masonry units, whereas CSEB masonry had an experimental inelastic behavior and cracks spread across all masonry constituents. This different behavior is likely because, in the FCB masonry walls, the masonry units are significantly stronger and have higher stiffness than the mortar and the unit-mortar interfaces, whereas the different masonry components have similar strength and stiffness in the CSEB masonry walls.

The FE simulation results indicate that simplified micro-modeling techniques can properly simulate the FE behavior for the FCB masonry shear walls. In fact, all three SMM approaches (i.e., SMM-I, SMM-II, and SMM-III) appear to provide similarly accurate results in terms of global load-displacement responses, peak loads (with errors contained between -4.08 and 15.26%), and initial stiffnesses (with errors contained between -11.40 and 6.29%). The models are less accurate in estimating the displacements at failure (with errors contained between -13.22% and 27.71%); however, this result may also be due to the lack of knowledge on the specific criterion used to terminate the experimental tests. It is observed that: (1) the computational costs increase from SMM-I to SMM-II and from SMM-II to SMM-III, (2) the accuracy in predicting the mechanical response of FCB masonry walls is similar for SMM-II and SMM-III and slightly better than SMM-I, and (3) the accuracy slightly degrades for increasing axial compression applied on the walls.

By contrast, these simplified micro-modeling techniques are in general not suitable for modeling the mechanical response of CSEB masonry walls, because they are unable to reproduce the failure mechanisms produced by cracks propagating across all masonry components. Therefore, a different modeling approach is needed to describe the

mechanical behavior of masonry walls and systems in which the different masonry components have similar strength and stiffness, as for CSEB masonry systems. A possible alternative that should be investigated in future studies is the use of a FE detailed micro-modeling approach, in which each component of a masonry system is modeled separately from the others through an appropriate nonlinear constitutive model.

Conflict of interest

The authors declare that they have no known competing financial interests or personal relationships that could have influenced or appeared to influence the work reported in this paper.

Acknowledgments

References

[1] Giambanco G, Di Gati L. A cohesive interface model for the structural mechanics of block masonry, Mechanics Research Communications, 1997; 24: 503–512. https://doi.org/10.1016/S0093-6413(97)00055-4.

[2] Giambanco G, Rizzo S, Spallino R. Numerical analysis of masonry structures via interface models, Computer Methods in Applied Mechanics and Engineering, 2001; 190: 6493–6511. https://doi.org/10.1016/S0045-7825(01)00225-0.

[3] Citto C. (2008). Two-dimensional interface model applied to masonry structures, MS thesis, University of Colorado, Denver, Colorado.

[4] Macorini L, Izzuddin BA. A non-linear interface element for 3d mesoscale analysis of brick-masonry structures, International Journal for Numerical Methods in Engineering, 2011; 85: 1584–1608. https://doi.org/10.1002/nme.3046.

[5] Kumar N, Barbato M. New constitutive model for interface elements in finite-element modeling of masonry, Journal of Engineering Mechanics, 2019; 145: 04019022. https://doi.org/10.1061/(ASCE)EM.1943-7889.0001592.

[6] Lourenço PB, Rots JG. Multisurface interface model for analysis of masonry structures, Journal of Engineering Mechanics, 1997; 123: 660–668. https://doi.org/10.1061/(ASCE)0733-9399(1997)123:7(660).

[7] Abdulla KF, Cunningham LS, Gillie M. Simulating masonry wall behaviour using a simplified micro-model approach, Engineering Structures, 2017; 151: 349–365. https://doi.org/10.1016/j.engstruct.2017.08.021.

[8] Pulatsu B, Erdogmus E, Lourenço PB, Lemos J V, Hazzard J. Discontinuum analysis of the fracture mechanism in masonry prisms and wallettes via discrete element method, Meccanica, 2020; 55: 505–523. https://doi.org/10.1007/s11012-020-01133-1 .

[9] Baraldi D, Cecchi A. A full 3d rigid block model for the collapse behaviour of masonry walls, European Journal of Mechanics - A/Solids, 2017; 64: 11–28. https://doi.org/10.1016/j.euromechsol.2017.01.012.

[10] Oliveira DV, Lourenço PB. Implementation and validation of a constitutive model for the cyclic behaviour of interface elements, Computers & Structures, 2004; 82: 1451–1461. https://doi.org/10.1016/j.compstruc.2004.03.041.

[11] D'Altri AM, Sarhosis V, Milani G, Rots J, Cattari S, Lagomarsino S, Sacco E, Tralli A, Castellazzi G, de Miranda S. Modeling strategies for the computational analysis of unreinforced masonry structures: review and classification, Archives of Computational Methods in Engineering, 2019; 1: 1–33. https://doi.org/10.1007/s11831-019-09351-x.

[12] Kumar N, Amirtham R, Pandey M. Plasticity based approach for failure modelling of unreinforced masonry, Engineering Structures, 2014; 80. https://doi.org/10.1016/j.engstruct.2014.08.021.

[13] Drougkas A, Roca P, Molins C. Experimental analysis and detailed micro-modeling of masonry walls subjected to in-plane shear, Engineering Failure Analysis, 2019; 95: 82–95. https://doi.org/10.1016/j.engfailanal.2018.08.030.

[14] Calderón S, Sandoval C, Arnau O. Shear response of partially-grouted reinforced masonry walls with a central opening: testing and detailed micro-modelling, Materials & Design, 2017; 118: 122–137. https://doi.org/10.1016/j.matdes.2017.01.019.

[15] Pourfalah S, Cotsovos DM, Suryanto B. Modelling the out-of-plane behaviour of masonry walls retrofitted with engineered cementitious composites, Computers & Structures, 2018; 201: 58–79. https://doi.org/10.1016/j.compstruc.2018.02.004.

[16] Page AWAW. Finite element model for masonry, Journal of the Structural Division, 1978; 104: 1267–1285. https://doi.org/10.1061/JSDEAG.0004969.

[17] Andreotti G, Graziotti F, Magenes G. Detailed micro-modelling of the direct shear tests of brick masonry specimens: the role of dilatancy, Engineering Structures, 2018; 168: 929–949. https://doi.org/10.1016/j.engstruct.2018.05.019.

[18] Sacco E, Toti J. Interface elements for the analysis of masonry structures, International Journal for Computational Methods in Engineering Science and Mechanics, 2010; 11: 354–373. https://doi.org/10.1080/15502287.2010.516793.

[19] Arnau O, Sandoval C, Murià-Vila D. Determination and validation of input parameters for detailed micro-modelling of partially grouted reinforced masonry walls, 10th Pacific Conference on Earthquake Engineering, vol. 68, 2015.

[20] Lourenço PB. (1996). Computational strategies for masonry structures, PhD Dissertation, Technische Universiteit Delft, Delft, Netherlands.

[21] Arya SK, Hegemier GA. On nonlinear response prediction of concrete masonry assemblies, Proceedings of the North American Masonry Conference, The Masonry Society, Boulder, Colorado, 1978, 11–19.

[22] Rots JG. Structural masonry, CRC Press, London, UK, 2021. https://doi.org/10.1201/9781003077961.

[23] Rots JG. Numerical simulation of cracking in structural masonry, Heron, 1991; 36: 49–63.

[24] Senthivel R, Lourenço PB. Finite element modelling of deformation characteristics of historical stone masonry shear walls, Engineering Structures, 2009; 31: 1930–1943. https://doi.org/10.1016/j.engstruct.2009.02.046.

[25] Miccoli L, Garofano A, Fontana P, Müller U. Experimental testing and finite element modelling of earth block masonry, Engineering Structures, 2015; 104: 80–94. https://doi.org/10.1016/j.engstruct.2015.09.020.

[26] Furukawa A, Spence R, Ohta Y, So E. Analytical study on vulnerability functions for casualty estimation in the collapse of adobe buildings induced by earthquake, Bulletin of Earthquake Engineering, 2010; 8: 451–479. https://doi.org/10.1007/s10518-009-9156-z.

[27] Tarque N. (2011). Numerical modelling of the seismic behaviour of adobe buildings, PhD Dissertation, Università Degli Studi Di Pavia, and Istituto Universitario Di Studi Superiori.

[28] Petracca M, Pelà L, Rossi R, Zaghi S, Camata G, Spacone E. Micro-scale continuous and discrete numerical models for nonlinear analysis of masonry shear walls, Construction and Building Materials, 2017; 149: 296–314. https://doi.org/10.1016/j.conbuildmat.2017.05.130.

[29] Vemuri J, Ehteshamuddin S, Kolluru S. Numerical simulation of soft brick unreinforced masonry walls subjected to lateral loads, Cogent Engineering, 2018; 5: 1–21. https:/doi.org/10.1080/23311916.2018.1551503.

[30] van Zijl GPAG. Modeling masonry shear-compression: role of dilatancy highlighted, Journal of Engineering Mechanics, 2004; 130: 1289–1296. https://doi.org/10.1061/(ASCE)0733-9399(2004)130:11(1289).

[31] Dolatshahi KM, Aref AJ. Two-dimensional computational framework of meso-scale rigid and line interface elements for masonry structures, Engineering Structures, 2011; 33: 3657–3667. https://doi.org/10.1016/j.engstruct.2011.07.030.

[32] Chisari C, Macorini L, Amadio C, Izzuddin BA. An inverse analysis procedure for material parameter identification of mortar joints in unreinforced masonry, Computers & Structures, 2015; 155: 97–105. https://doi.org/10.1016/j.compstruc.2015.02.008.

[33] Zhang Y, Macorini L, Izzuddin BA. Mesoscale partitioned analysis of brick-masonry arches, Engineering Structures, 2016; 124: 142–166. https://doi.org/10.1016/j.engstruct.2016.05.046.

[34] Chisari C, Macorini L, Amadio C, Izzuddin BA. Identification of mesoscale model parameters for brick-masonry, International Journal of Solids and Structures, 2018; 146: 224–240. https://doi.org/10.1016/j.ijsolstr.2018.04.003.

[35] Minga E, Macorini L, Izzuddin BA. A 3d mesoscale damage-plasticity approach for masonry structures under cyclic loading, Meccanica, 2018; 53: 1591–1611. https://doi.org/10.1007/s11012-017-0793-z.

[36] Alfano G, Sacco E. Combining interface damage and friction in a cohesive-zone model, International Journal for Numerical Methods in Engineering, 2006; 68: 542–582. https://doi.org/10.1002/nme.1728.

[37] Parrinello F, Failla B, Borino G. Cohesive–frictional interface constitutive model, International Journal of Solids and Structures, 2009; 46: 2680–2692. https://doi.org/10.1016/j.ijsolstr.2009.02.016.

[38] Formica G, Sansalone V, Casciaro R. A mixed solution strategy for the nonlinear analysis of brick masonry walls, Computer Methods in Applied Mechanics and Engineering, 2002; 191: 5847–5876. https://doi.org/10.1016/S0045-7825(02)00501-7.

[39] Gambarotta L, Lagomarsino S. Damage models for the seismic response of brick masonry shear walls. part i: the mortar joint model and its applications, Earthquake Engineering & Structural Dynamics, 1997; 26: 423–439. https:/doi.org/10.1002/(SICI)1096-9845(199704)26:4%3C423::AID-EQE650%3E3.0.CO;2-%23.

[40] Greco F, Leonetti L, Luciano R, Trovalusci P. Multiscale failure analysis of periodic masonry structures with traditional and fiber-reinforced mortar joints, Composites Part B: Engineering, 2017; 118: 75–95. https://doi.org/10.1016/j.compositesb.2017.03.004.

[41] Chaimoon K, Attard MM. Modeling of unreinforced masonry walls under shear and compression, Engineering Structures, 2007; 29: 2056–2068. https://doi.org/10.1016/j.engstruct.2006.10.019.

[42] Shing PB, Manzouri T. Analysis of unreinforced masonry structures using elastic/viscoplastic models, Sísmica 2004–6° Congresso Nacional de Sismologia e Engenharia Sísmica Livro de Actas, Universidade Do Minho, Guimaraes, Portugal, 2004, 137–150.

[43] Dolatshahi KM, Nikoukalam MT, Beyer K. Numerical study on factors that influence the in-plane drift capacity of unreinforced masonry walls, Earthquake Engineering & Structural Dynamics, 2018; 47: 1440–1459. https://doi.org/10.1002/eqe.3024.

[44] Dolatshahi KM, Yekrangnia M. Out-of-plane strength reduction of unreinforced masonry walls because of in-plane damages, Earthquake Engineering & Structural Dynamics, 2015; 44: 2157–2176. https://doi.org/10.1002/eqe.2574.

[45] Dolatshahi KM, Aref AJ. Multi-directional response of unreinforced masonry walls: experimental and computational investigations, Earthquake Engineering & Structural Dynamics, 2016; 45: 1427–1449. https://doi.org/10.1002/eqe.2714.

[46] Aref AJ, Dolatshahi KM. A three-dimensional cyclic meso-scale numerical procedure for simulation of unreinforced masonry structures, Computers & Structures, 2013; 120: 9–23. https://doi.org/10.1016/j.compstruc.2013.01.012.

[47] Bolhassani M, Hamid AA, Lau ACW, Moon F. Simplified micro modeling of partially grouted masonry assemblages, Construction and Building Materials, 2015; 83: 159–173. https://doi.org/10.1016/j.conbuildmat.2015.03.021.

[48] Tang C, Shi B, Gao W, Chen F, Cai Y. Strength and mechanical behavior of short polypropylene fiber reinforced and cement stabilized clayey soil, Geotextiles and Geomembranes, 2007; 25: 194–202. https://doi.org/10.1016/j.geotexmem.2006.11.002.

[49] Aghababaie Mobarake A, Khanmohammadi M, Mirghaderi SR. A new discrete macro-element in an analytical platform for seismic assessment of unreinforced masonry buildings, Engineering Structures, 2017; 152: 381–396. https://doi.org/10.1016/j.engstruct.2017.09.013.

[50] Caliò I, Marletta M, Pantò B. A new discrete element model for the evaluation of the seismic behaviour of unreinforced masonry buildings, Engineering Structures, 2012; 40: 327–338. https://doi.org/10.1016/j.engstruct.2012.02.039.

[51] Baraldi D, Cecchi A. Discrete approaches for the nonlinear analysis of in plane loaded masonry walls: molecular dynamic and static algorithm solutions, European Journal of Mechanics - A/Solids, 2016; 57: 165–177. https://doi.org/10.1016/j.euromechsol.2015.12.008.

[52] Bui T-T, Limam A, Sarhosis V. Failure analysis of masonry wall panels subjected to in-plane and out-of-plane loading using the discrete element method, European Journal of Environmental and Civil Engineering, 2019; 1: 1–17. https://doi.org/10.1080/19648189.2018.1552897.

[53] Cuellar-Azcarate MC. (2016). Engineered earthen masonry structures for extreme wind loads, PhD Dissertation, University of South Carolina, Columbia, South Carolina.

[54] Jaquin P. History of earth building techniques, Modern Earth Buildings: Materials, Engineering, Constructions and Applications, 2012, 307–323. https://doi.org/10.1533/9780857096166.3.307.

[55] Kumar N, Barbato M, Holton R. Feasibility study of affordable earth masonry housing in the U.S. Gulf Coast region, Journal of Architectural Engineering, 2018; 24. https://doi.org/10.1061/(ASCE)AE.1943-5568.0000311.

[56] Ben-Alon L, Loftness V, Harries KA, Hameen EC, Bridges M. Integrating earthen building materials and methods into mainstream construction, Journal of Green Building, 2020; 15: 87–106. https://doi.org/10.3992/1943-4618.15.1.87.

[57] Matta F, Cuellar-Azcarate MC, Garbin E, Cuéllar-Azcárate MC, Garbin E. Earthen masonry dwelling structures for extreme wind loads, Engineering Structures, 2015; 83: 163–175. https://doi.org/10.1016/j.engstruct.2014.10.043.

[58] Atkinson RH, Amadei BP, Saeb S, Sture S. Response of masonry bed joints in direct shear, Journal of Structural Engineering, 1989; 115: 2276–2296. https://doi.org/10.1061/(ASCE)0733-9445(1989)115:9(2276).

[59] Hofmann P, Stockl S. Tests on the shear-bond behaviour in the bed-joints of masonry, Masonry Int, 1986; 9: 1–15.

[60] Van der Pluijm R. Shear behaviour of bed joints, Proceedings of 6th North American Masonry Conference, The Masonry Society, Boulder, Colorado, 1993, 125–136.

[61] Van der Pluijm R. Overview of deformation controlled combined tensile and shear tests, Eindhoven University of Technology, Eindhoven, The Netherlands, 1998, vol. Technical.

[62] Page AW. The biaxial compressive strength of brick masonry, Proceedings of the Institution of Civil Engineers, 1981; 71: 893–906. https://doi.org/10.1680/iicep.1981.1825.

[63] Page AW. The strength of brick masonry under biaxial tension-compression, International Journal of Masonry Construction, 1983; 3: 26–31.

[64] Andreaus U. Failure criteria for masonry panels under in-plane loading, Journal of Structural Engineering, 1996; 122: 37–46. https://doi.org/10.1061/(ASCE)0733-9445(1996)122:1(37).

[65] Roberts JJ, Edgel GJ, Rathbone AJ. BS 5628:1985: British standard code of practice for use of masonry part 2: structural use of reinforced and prestressed masonry, Palladian Publications Limited, London, UK, 2018. https://doi.org/10.1201/9781482275636.

[66] Pelà L. (2009). Continuum damage model for nonlinear analysis of masonry structures, PhD Dissertation, Universitat Politècnica de Catalunya, Catalonia, Spain, & Università Degli Studi Di Ferrara, Italy.

[67] Dassault Systèmes. Abaqus 6.13 documentation, Dassault Systèmes, Providence, RI, 2013.

[68] Lubliner J, Oliver J, Oller S, Oñate E. A plastic-damage model for concrete, International Journal of Solids and Structures, 1989; 25: 299–326. https://doi.org/10.1016/0020-7683(89)90050-4.

[69] Lee J, Fenves GL. Plastic-damage model for cyclic loading of concrete structures, Journal of Engineering Mechanics, 1998; 124: 892–900. https://doi.org/10.1061/(ASCE)0733-9399(1998)124:8(892).

[70] ASTM International. ASTM C952-12 (withdrawn 2018) standard test method for bond strength of mortar to masonry units, ASTM Standards, ASTM International, West Conshohocken, PA, 2012. https://doi.org/10.1520/C0952-12.

[71] ASTM International. ASTM C1314-21 standard test method for compressive strength of masonry prisms, ASTM Standards, ASTM International, West Conshohocken, PA, 2021. https:/doi.org/10.1520/C1314-21.

[72] Lourenço PB, Almeida JC, Barros JAO. Experimental investigation of bricks under uniaxial tensile testing, Journal of British Masonry Society Masonry International, 2005; 18: 11–20.

[73] Masonry Standards Joint Committee. TMS 402/602-16 Building code requirements and specification for masonry structures, The Masonry Society, Boulder, Colorado, 2016. ISBN: 978-1-929081-52-3.

[74] Jankowiak T, Lodygowski T. Identification of parameters of concrete damage plasticity constitutive model, Foundations of Civil and Environmental Engineering, 2005; 6: 53–69.

[75] Michał S, Andrzej W. Calibration of the CDP model parameters in ABAQUS, The 2015 World Congress on Advances in Structural Engineering and Mechanics (ASEM15), 2015.

[76] Hughes TJR. The finite element method: linear static and dynamic finite element analysis, Courier Corporation, 2012. ISBN:0486135020.

[77] Wu SR, Gu L. Introduction to the explicit finite element method for nonlinear transient dynamics, Wiley, 2012. https://doi.org/10.1002/9781118382011.

[78] Ferrante A, Clementi F, Milani G. Dynamic behavior of an inclined existing masonry tower in Italy, Frontiers in Built Environment, 2019; 5: 33. https://doi.org/10.3389/fbuil.2019.00033.

[79] Silva LC, Lourenço PB, Milani G. Numerical homogenization-based seismic assessment of an english-bond masonry prototype: structural level application, Earthquake Engineering & Structural Dynamics, 2020; 49: 841–862. https://doi.org/10.1002/eqe.3267.

[80] Simo JC, Hughes TJR. Computational inelasticity, Springer-Verlag, New York, USA, 1998, vol. 7. https://doi.org/10.1007/b98904.

[81] Newmark NM. A method of computation for structural dynamics, Journal of the Engineering Mechanics Division, 1959; 85: 67–94. https://doi.org/10.1061/JMCEA3.0000098.

[82] Chopra AKCA. Dynamics of structures : theory and applications to earthquake engineering, Pearson, Boston, Massachusetts, USA, 2014, 4th ed. ISBN:0273774247.

[83] Anthoine A. Homogenization of periodic masonry: plane stress, generalized plane strain or 3d modelling?, Communications in Numerical Methods in Engineering, 1997; 13: 319–326. https://doi.org/10.1002/(SICI)1099-0887(199705)13:5<319::AID-CNM55>3.0.CO;2-S.

[84] Addessi D, Sacco E. Nonlinear analysis of masonry panels using a kinematic enriched plane state formulation, International Journal of Solids and Structures, 2016; 90: 194–214. https://doi.org/10.1016/j.ijsolstr.2016.03.002.

[85] Vermeltfoort AT, Raijmakers TMJ. Deformation controlled tests in masonry shear walls, part 2 (in Dutch), Technische Universiteit Delft, Eindhoven, The Netherlands, 1993.

[86] Raijmakers TMJ, Vermeltfoort AT. Deformation controlled tests in masonry shear walls (in dutch), Technische Universiteit Delft, Eindhoven, The Netherlands, 1992.

[87] Kupfer HB, Gerstle KH. Behavior of concrete under biaxial stresses, Journal of the Engineering Mechanics Division, 1973; 99: 853–866. https://doi.org/10.1061/JMCEA3.0001789.

[88] Hendry AW. Structural masonry, Scholium International, London, UK, 1998, 2nd ed. ISBN:134914827X.

[89] D'Altri AM, Sarhosis V, Milani G, Rots J, Cattari S, Lagomarsino S, Sacco E, Tralli A, Castellazzi G, de Miranda S. A review of numerical models for masonry structures, Numerical Modeling of Masonry and Historical Structures, Elsevier, 2019, 3–53. https://doi.org/10.1016/B978-0-08-102439-3.00001-4.

[90] Danso H, Akwaboah M. Assessment of the quality of burnt bricks produce in Ghana: the case of Ashanti region, Case Studies in Construction Materials, 2021; 15: e00708.

[91] Rengifo-López EL, Kumar N, Matta F, Barbato M. Experimental and numerical study of uniaxial compression behavior of compressed and stabilized earth blocks, Proceedings of the 13th North American Masonry Conference, The Masonry Society, Longmont, Colorado, 2019, 925–936. ISBN:1053-2366.

[92] Rengifo-López EL, Kumar N, Matta F, Barbato M. Experimental characterization and numerical simulation of compressive behavior of compressed and stabilized earth block specimens, Proceedings for the Tenth International Earthbuilding Conference (Earth USA 2019), Adobe in Action, La Madera, New Mexico, 2019, 314–320.